NANO LETTERS

Letter

pubs.acs.org/NanoLett

IR Near-Field Spectroscopy and Imaging of Single Li_xFePO_4 Microcrystals

I. T. Lucas,[†,#,⊥] A. S. McLeod,[‡,⊥] J. S. Syzdek,[†] D. S. Middlemiss,[§] C. P. Grey,[§,∥] D. N. Basov,[‡] and R. Kostecki*[,†]

[†]Lawrence Berkeley National Laboratory, Berkeley, California 94720, United States

[‡]Department of Physics, University of California, San Diego, La Jolla, California 92093, United States

[§]Department of Chemistry, University of Cambridge, Cambridge CB2 1EW, United Kingdom

[∥]Department of Chemistry, Stony Brook University, Stony Brook, New York 11794-3400, United States

[#]UPMC Univ Paris 06, Sorbonne Universités, UMR 8235, LISE, Paris, F-75252, France

Supporting Information

ABSTRACT: This study demonstrates the unique capability of infrared near-field nanoscopy combined with Fourier transform infrared spectroscopy to map phase distributions in microcrystals of Li_xFePO_4, a positive electrode material for Li-ion batteries. Ex situ nanoscale IR imaging provides direct evidence for the coexistence of $LiFePO_4$ and $FePO_4$ phases in partially delithiated single-crystal microparticles. A quantitative three-dimensional tomographic reconstruction of the phase distribution within a single microcrystal provides new insights into the phase transformation and/or relaxation mechanism, revealing a $FePO_4$ shell surrounding a diamond-shaped $LiFePO_4$ inner core, gradually shrinking in size and vanishing upon delithiation of the crystal. The observed phase propagation pattern supports recent functional models of $LiFePO_4$ operation relating electrochemical performance to material design. This work demonstrates the remarkable potential of near-field optical techniques for the characterization of electrochemical materials and interfaces.

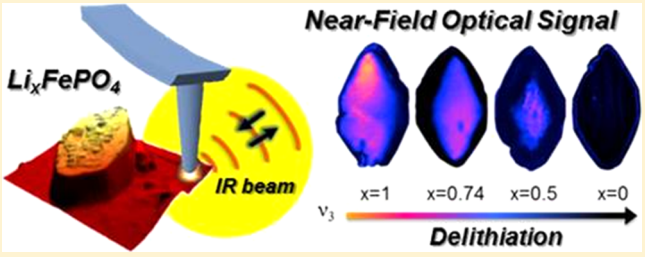

KEYWORDS: *IR s-SNOM, $LiFePO_4$, phase distribution, Li-ion batteries*

Infrared apertureless near-field scanning optical microscopy (IR s-SNOM) was applied to resolve the operational mechanism of $LiFePO_4$ (LFP), a positive electrode material used in commercially viable Li-ion batteries. Although LFP is known to convert to $FePO_4$ (FP) at 3.4 V versus Li^+/Li^0 via a first-order phase transition, at least in micron-sized particles,[1] the specific functional mechanism of $LiFePO_4$ (de)lithiation during battery charge/discharge is still under debate. To enhance extensive studies conducted on composite electrodes, control experiments on model samples must be carefully designed and carried out to reliably probe chemical composition variations within single Li_xFePO_4 particles with different lithium contents at high spatial (nanometer) resolution and with adequate chemical specificity.[2] The present study demonstrates the potential of IR s-SNOM[3] imaging and broadband nanospectroscopy (nano-FTIR) for chemical and structural characterization of Li_xFePO_4 single particles.

Most conventional analytical techniques employed to study fine changes in the local composition of Li_xFePO_4 single particles offer limited descriptions of the reaction mechanism, providing sensitivity only to long-range order (X-ray and electron diffraction, transmission electron microscopy),[4−9] suffering from spectral overlap among elements (electron energy loss spectroscopy, EELS)[10,11] or poor contrast in very thin samples (transmission X-ray microscopy, TXM)[12,13] with the concurrent possibility of beam damage from highly energetic particles or photons. Vibrational spectroscopies sensitive to lattice vibrations are of particular interest because the IR/Raman spectral signatures of $LiFePO_4$, $FePO_4$, and their metastable intermediates $Li_{0.34}FePO_4$ and $Li_{0.66}FePO_4$ provide excellent chemical contrast.[14,15] However, the diffraction-limited spatial resolution of conventional far-field optical techniques presents a serious barrier to studying the structure and chemical composition of submicrometer specimens used in commercial batteries.

IR s-SNOM is still an emerging near-field imaging and spectroscopic technique, both theory and practice undergoing rapid and promising development.[16] Recent technical improvements including lock-in detection of the optical signal, effective far-field background suppression schemes,[17,18] and powerful quantum cascade or pulsed broadband IR laser light sources[19−21] have enabled local characterization of well-defined organic and inorganic nanomaterials with high sensitivity and specificity,[22] and at sub-picosecond temporal resolutions.[23]

Received: March 23, 2014
Revised: September 25, 2014
Published: November 6, 2014

The high spatial resolution afforded by IR s-SNOM is determined by the radius of curvature at the atomic force microscopy (AFM) tip apex (<30 nm), independent of the free-space wavelength of the illuminating light. The technique operates through extreme polarization sensitivity of a sharp conductive probe to the optical properties of a sampling volume near the probe apex. Upon illumination, the electrically polarized probe tip generates a spatially extended evanescent near-field, which can penetrate a few tens of nanometers deep into IR-transparent samples.[24,25] The tip-enhanced near-field couples locally to resonant phonon modes of the sample and enables detection of subsurface objects, provided that they are located within the subwavelength sampling volume of the near-field probe. The structural and compositional specificity of IR near-field spectroscopy is analogous to far-field vibrational spectroscopies.[22]

$LiFePO_4$ single microcrystals ($4 \times 2 \times 0.4$ μm along the *c*, *a*, and *b* directions, respectively) exhibiting hexagonal platelet geometry were selected for ex situ IR s-SNOM studies.[7] Figure 1 shows SEM micrographs of representative $LiFePO_4$ and

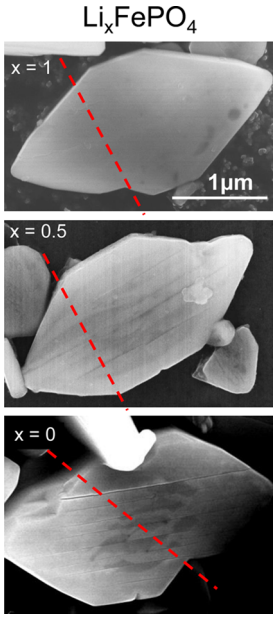

Figure 1. Scanning electron micrographs of single $LiFePO_4$, $Li_{0.5}FePO_4$, and $FePO_4$ microcrystals, revealing cracks along the crystal surface after delithiation.

chemically delithiated single crystals with average compositions of $Li_{0.5}FePO_4$ and $FePO_4$. Near-field nano-FTIR (nano-scale Fourier transform infrared) spectra were acquired from single FP and LFP particles and compared with conventional far-field FTIR transmission spectra of the same batch of crystals (see Supporting Information)[15,26,27]

The second harmonic amplitude S_2 (see Methods) nano-FTIR spectra (Figure 2a) reveal strong surface phonon modes at 950−1150 cm^{-1} attributable to intramolecular symmetric (ν_1) and asymmetric (ν_3) stretching vibrations of the PO_4^{3-} anions, which are also clearly resolved in far-field FTIR spectra.[15] However, the signature peaks of these phonon modes appear sharpened and red shifted in the near-field spectra as compared with their far-field counterparts.[28−31] The observed near-field resonance effect results in a backscattering response that is highly sensitive to phonon oscillator strengths, inducing

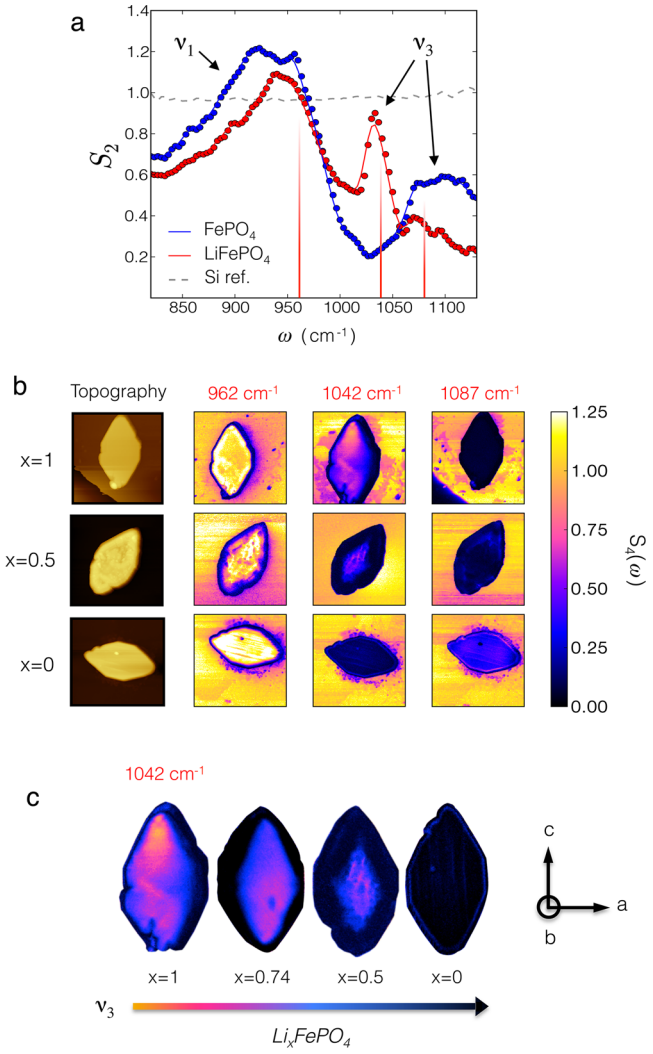

Figure 2. (a) Nano-FTIR S_2 spectra (2nd harmonic amplitude of the backscattered field) of pure-phase $LiFePO_4$ and $FePO_4$ microcrystals with symmetric (ν_1) and antisymmetric (ν_3) vibrational modes indicated (comparison with far-field FTIR transmission spectra is presented in Supporting Information); a typical 100% line acquired from the silicon substrate and used for reference is also shown (Si ref.) (b) AFM topography and corresponding infrared near-field amplitude S_4 (4th harmonic) images acquired at 1087, 1042, and 962 cm^{-1} for $LiFePO_4$, $Li_{0.5}FePO_4$, and $FePO_4$ crystals; (c) S_4 images highlighting the phase distribution and propagation of lithiated/delithiated phases in $LiFePO_4$, $Li_{0.74}FePO_4$, $Li_{0.5}FePO_4$, and $FePO_4$ crystals.

strong contrasts in spectral intensity between adjacent modes. LFP and FP share several surface phonon modes in the 950−1150 cm^{-1} spectral range. However, the nano-FTIR spectrum of LFP exclusively exhibits a strong phonon mode near 1042 cm^{-1} that corresponds to the asymmetric (ν_3) stretch of the PO_4^{3-} anion. DFT calculations attribute the increased oscillator strength and frequency red shift of the ν_3 mode in LFP as compared with FP to a redistribution of electron density between the P−O_1 and P−O_2 bonds within the symmetry-distinct oxygen sublattices of the PO_4^{3-} anions (see Supporting Information).[32,33]

IR s-SNOM imaging of $LiFePO_4$ and partially and fully delithiated Li_xFePO_4 (x = 1, 0.5 and 0.0) microcrystals was realized with the fourth harmonic amplitude S_4 signal at three distinct IR excitation frequencies, 962, 1042, and 1087 cm^{-1}

dx.doi.org/10.1021/nl5010898 | *Nano Lett.* 2015, 15, 1−7

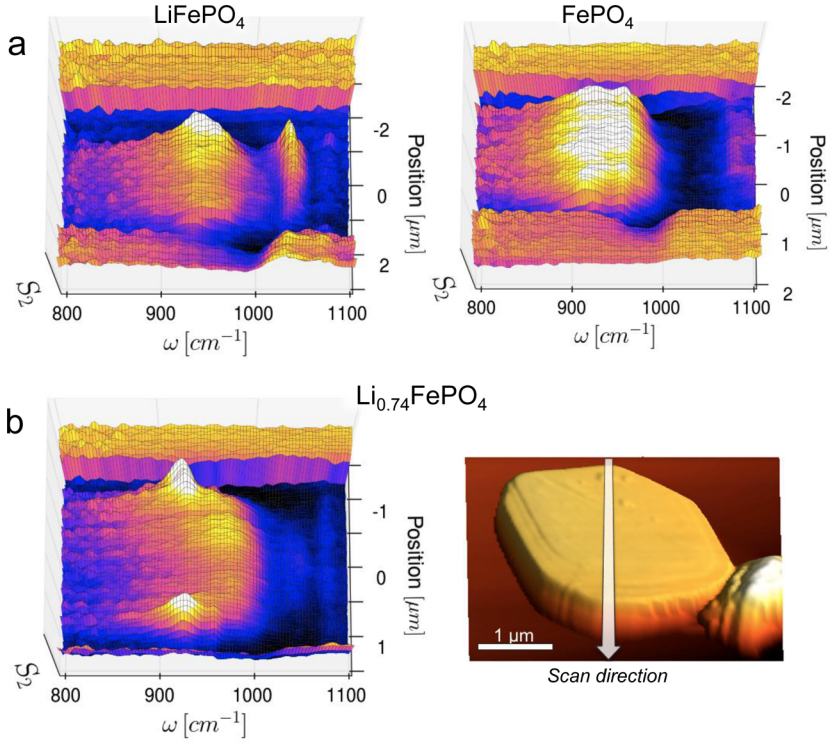

Figure 3. (a) Position-resolved nano-FTIR S_2 spectra acquired along the surface of two pure-phase microcrystals and (b) along a partially delithiated $Li_{0.74}FePO_4$ crystal (color scale identical to that in Figure 2b). An AFM topography image (false color height) displays the $Li_{0.74}FePO_4$ crystal and location of the nano-FTIR line-scan.

provided by a tunable quantum cascade laser (Figure 2b). The observed S_4 image contrasts are associated with different phonon coupling efficiencies in LFP and FP at the given excitation frequencies and correspond to variations of local crystal structure and/or composition. The sudden drop of signal at the particle boundary originates from loss of tip−sample coupling at the steep crystal edges.

The IR s-SNOM images collected at 962 cm^{-1} display poor LFP/FP/silicon substrate contrast due to their comparable S_4 signal intensity at this frequency. On the other hand, the images of partially delithiated $Li_{0.5}FePO_4$ at 1042 and 1087 cm^{-1} reveal a diamond-shaped region in the middle of the crystal, which was also observed in the corresponding near-field phase images (see Supporting Information, Figure S3). AFM topography images show no indication that the observed chemical contrast could originate from variations in surface morphology. Interestingly, reverse optical contrast observed in the images of $Li_{0.5}FePO_4$ crystals at 1042 and 1087 cm^{-1} reveals strong coupling to the ν_3 phonon mode in LFP and FP, respectively (Figure 2a).

The observed shrinking of the central diamond-shaped region in another delithiated crystal with higher lithium content, $Li_{0.74}FePO_4$ versus $Li_{0.5}FePO_4$ (Figure 2c), indicates a progressive evolution of an outer FP-rich region at the expense of the inner LFP-core upon delithiation. The continuous and monotonic variation in observable fill fractions of putative LFP and FP phases as a function of Li content further supports the respective identification of inner and outer regions in Li_xFePO_4 particles with Li-rich and Li-poor regions, respectively. These observations provide direct evidence for the coexistence of LFP and FP phases within individual Li_xFePO_4 microcrystals, as previously inferred from two-dimensional (2D) chemical mapping of thin single crystal particles[13] using scanning and full-field transmission X-ray microscopy coupled to absorption near edge spectroscopy (STXM- and FF TXM-XANES).

A series of nano-FTIR spectra acquired across the $a-c$ surface of pure-phase LFP and FP crystals (Figure 3a) appear consistent with the reference spectra displayed in Figure 2a. Remarkably, the scan across the partially delithiated $Li_{0.74}FePO_4$ crystal (Figure 3b) displays spectral patterns characteristic of an outer Li-depleted zone and a Li-rich region near the crystal center. However, the $Li_{0.74}FePO_4$ spectra do not replicate exactly the reference nano-FTIR spectra for pure-phase LFP or FP (Figure 2a) except for the locations close to the edges of the crystal, which exhibit characteristics of pure FP.

The relative IR near-field intensity of the ν_3 mode is noticeably smaller throughout $Li_{0.74}FePO_4$ as compared with pure LFP, yet its frequency remains fairly constant at 1042 ± 5 cm^{-1}. This observation appears inconsistent with the presence of a stable homogeneous solid solution[1,4,8,34,35] at an intermediate state of delithiation. To test this hypothesis, a member of the solid solution Li_xFePO_4 with composition $Li_{0.6}FePO_4$ was investigated by conventional FTIR spectroscopy (see Supporting Information, Figure S2). A continuous shift of the ν_3 mode in the far-field FTIR spectrum of Li_xFePO_4 is realized for such a solid solution, varying with the mean Fe oxidation state, rather than a superposition of the LFP and FP ν_3 mode characteristics. Therefore, solid solution phases are either completely absent in the Li_xFePO_4 microcrystals examined by nano-FTIR or their local concentration is below the detection limit of the IR near-field probe.

On the other hand, the decrease in near-field signal intensity of the ν_3 mode at 1042 cm^{-1} in the $Li_{0.74}FePO_4$ crystal center is ascribed to the presence of the $LiFePO_4$ inner core buried under a $FePO_4$ outer layer. Thus, the observed ν_3 mode

dx.doi.org/10.1021/nl5010898 | Nano Lett. 2015, 15, 1−7

intensity variations can be used to determine the local volume ratio and geometric configuration of LFP and FP phases.

The tomographic capabilities of IR s-SNOM to image structures buried beneath thick (<100 nm) layers of IR transparent material or to characterize phonon-resonant SiO_2 layers have been demonstrated in previous studies.[24,25] To reveal the 3D phase distribution in Li_xFePO_4 microcrystals nano-FTIR spectra were matched with theoretical predictions obtained from the lightning rod model of near-field interactions between the probe and sample (see Methods). The lightning rod model accounts for the strong dependence of optical reflections from layered structures on the momentum decomposition of incident light.[31]

This model was used to extract the surface reflection coefficients $\beta_{LFP}(\omega)$ and $\beta_{FP}(\omega)$ for the LFP and FP by reproduction of their reference nano-FTIR spectra (Figure 2a). The calculated pure-phase reflection coefficients were then used to approximate the composite optical response of a model three-layer FP/LFP/FP composite structure.[36] The resultant model spectra (Figure 4a) were matched with the experimental near-field S_2 spectra of the $Li_{0.74}FePO_4$ microcrystal to determine the ν_3 mode amplitude measured in S_2 at 1040 cm^{-1} across the width of a $Li_{0.74}FePO_4$ crystal and local thicknesses t_{LFP} of the LFP interlayer. The corresponding reconstruction of the internal compositional profile is shown in Figure 4c.

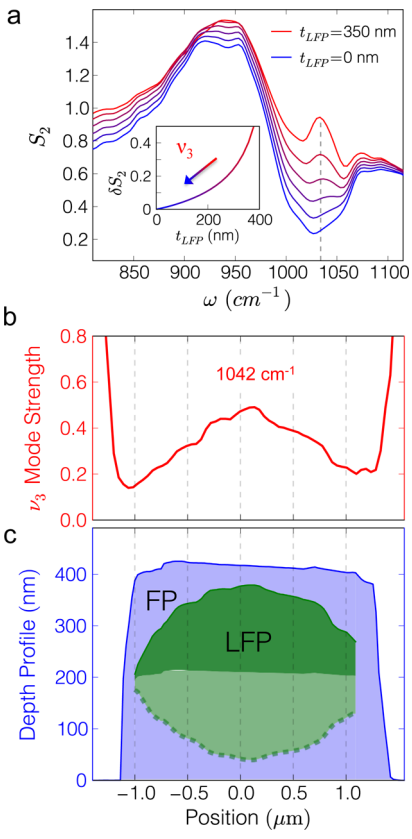

Figure 4. (a) Theoretical near-field S_2 spectra of a partially delithiated $LiFePO_4$ microcrystal computed using the lighting rod model of probe-sample near-field interaction (see text) as a function of the LFP core thickness, (b) the ν_3 mode amplitude measured in S_2 at 1040 cm^{-1} across the width of a $Li_{0.74}FePO_4$ crystal, and (c) the corresponding reconstruction of the internal compositional profile (FP in blue, LFP in green).

The corresponding values of t_{LFP} were then used to reconstruct an idealized tomographic 3D phase composition image of the crystal as schematically depicted in Figure 5. Such an inverse analysis of nano-FTIR spectra constitutes a successful example of near-field tomographic analysis of functional materials.

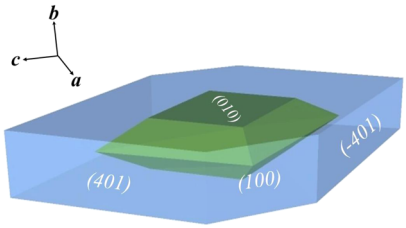

Figure 5. Schematic depiction of the FP–LFP–FP core/shell structure inferred from the near-field tomography analysis (see text).

The depth sensitivity of IR s-SNOM is sufficient in this case to probe at depths exceeding 100 nm into the $Li_{0.74}FePO_4$ microcrystal due to the IR-transparent character of FP and to the long-range nature of near-field interactions with the LFP ν_3 phonon near 1040 cm^{-1}. This phenomenon effectively enables phonon-enhanced near-field optical tomography (see Supporting Information). However, sensitivity to variations in the lithiated core's lower portion is virtually nonexistent, and the presented extrapolation of the phase distribution in the bottom part of the crystal (lighter green area in Figure 4b) is a simple ansatz of symmetric delithiation. Because the depth of the tip's probing electric field scales inversely with its confinement, uncertainty in the LFP thickness extraction corresponds with that of the tip's radius of curvature, which in this case was assumed at 25 nm (due to wear, slightly more blunt than the nominal value; see Methods section). Detailed discussion of uncertainties in the tomographic reconstruction is presented in the Supporting Information.

While t_{LFP} is essentially zero (complete delithiation) at the $Li_{0.74}FePO_4$ particle edges, t_{LFP} reaches ~350 nm at the particle center. Interestingly, the observed diamond-shaped LFP core does not replicate the contours of the crystal, that is, the original orientation of the edges and facets. The central approximately diamond-shaped domain of LFP (Figure 2c) shrinks as the average stoichiometry proceeds from $Li_{0.74}FePO_4$ to $Li_{0.5}FePO_4$, and disappears completely at the end of the delithiation process. However, the observed phase transformation mechanism does not follow a simple core–shell model, as phase boundaries appear to form at specific orientations. However, considering the limited spatial resolution of IR s-SNOM and inherent experimental error and uncertainty it is impossible to determine their exact crystallographic directions. This may indicate a complex delithiation–relaxation mechanism in $Li_{0.74}FePO_4$, which can affect the local Li^+ transport rate and promote LFP/FP phase boundary propagation along specific directions.

Like many binary systems, Li_xFePO_4 is likely to phase segregate into a mixture of two immiscible phases: heterosite $Fe^{III}PO_4$ and triphylite $LiFe^{II}PO_4$ across a large compositional range ($0.05 < x < 0.89$).[1] Coexistence of pure LFP and FP or $Li_\alpha FePO_4$ and $Li_{1-\beta}FePO_4$, intermediate phases in Li_xFePO_4 composite electrodes, have already been reported.[6,7,10,11,13,35,37–39] However, the exact phase distribution within a single Li_xFePO_4 microcrystal as revealed by IR s-

dx.doi.org/10.1021/nl5010898 | Nano Lett. 2015, 15, 1–7

SNOM 3D tomography has only been directly resolved in the present study. Viewed in the context of the previously proposed axial[7] or mosaic[37] phase distribution models, a radial distribution (core−shell structure)[10,35,39−41] appears to best support our observations.

Ex situ EELS measurements of chemically delithiated Li_xFePO_4 microparticles showed that Li^+ is removed preferentially from surface regions.[11] On the other hand, Li_xFePO_4 nanoparticles can accommodate the lattice mismatch between LFP and FP frameworks and the resulting elastic strain by locating the phase with smaller unit-cell volume, that is, $FePO_4$ at the particle core.[10,11,42,43] Elastic relaxation near surfaces leads to the formation of the characteristic stripes along the *c*-axis morphology.[7,44] However, high-resolution ptychographic images of submicron Li_xFePO_4 particles showed an internal chemical domain pattern between $LiFePO_4$ and $FePO_4$ revealing coexistence of two phases very similar to that observed here.[45]

In larger microcrystals, the ratio of surface energy to elastic energy is lower, and internal strain may be relieved through the formation of dislocations, cracks, and voids, explaining why such a nucleation and phase propagation mechanism may not be universal. In fact, the partially and fully delithiated microcrystals examined in this study exhibit surface cracks along the *c*-axis (Figure 1). Although these surface imperfections appear disconnected from the LFP and FP phase distribution patterns observed in the IR s-SNOM images (Figure 2b), the rate and direction of the phase boundary movement upon delithiation may be affected by the formation of these structural defects.[13]

The large chemical potential gradient of Li^+ together with the stress developed at the interface between incommensurate LFP and FP lattices may provide the driving force for phase boundary propagation.[6,46] Anisotropic elastic stiffness and misfit strains lead to formation of low-energy phase boundaries along [101] planes, whereas other phase boundary orientations can originate from a partial loss of coherency in the [100] direction.[44] Ramana et al.[9] observed LFP regions in partially delithiated particles exhibiting phase boundaries propagating not only along the [101] direction, but also along the *c*- and *a*-directions. These additional interfaces are responsible for maintaining the domain's finite cross-sectional size in the *ac*-plane. However, their study revealed nothing about the size of domains along the *b*-direction.

Bazant et al. have applied a quantitative phase field theory[42,44,47,48] of nucleation taking account of surface energies, electrochemical potential, and elastic energy to model intercalation waves propagating inward from the side facets while bending from coherency strain upon lithiation of single-crystal $FePO_4$ 150 × 76 nm nanoparticles.[42] This approach produced a central diamond-shaped lithium-depleted zone, which comprises a mirror image of the Li_xFePO_4 microcrystal structure observed experimentally in this work. The striking similarity of these theoretical and experimental results may suggest similar coherency strain-controlled mechanism of phase propagation in Li_xFePO_4 micron-sized particles upon lithiation and delithiation processes.

On the other hand, Malik et al. have suggested that classical nucleation and growth theory is an implausible mechanism for lithiation.[38] Instead, they have proposed a single-phase nonequilibrium overpotential-driven mechanism involving the presence of solid solutions. In their proposed framework, a particle transforms from LFP to FP via a solid solution. However, if the transformation is interrupted and the potential is removed, the Li_xFePO_4 particle will, if sufficiently small, react to form either LFP or FP only, taking up or giving Li^+ to the solution and nearby particles. For larger particles, where LFP/FP phase boundaries can exist within the same particle,[7,8] rapid relaxation will occur to form an energetically favorable distribution of LFP and FP phases (which minimize strain and chemical potential gradients). The resultant phase boundaries need not lie along main crystallographic orientations. Chemical delithiation may trigger the formation of a solid solution at the LFP/FP interphase providing sufficient overpotential to facilitate this theoretically predicted pathway.[38,47,49] The transition between the nanoparticle and micron-sized regimes is unclear and LFP and FP interfaces have been observed to exist in particles as small as 200 nm.[13] Liu et al. demonstrated the formation of a nonequilibrium solid solution phase Li_xFePO_4 ($0 < x < 1$) in nanoparticulate composite electrodes. High-rate cycling produced compositions spanning the entire composition between end thermodynamic phases, $LiFePO_4$ and $FePO_4$, via a continuous change in structure rather than a distinct moving phase boundary between $LiFePO_4$ and $FePO_4$.[50] Similar results were observed by Zhang et al.[51] Bai et al. have proposed that formation of a solid solution phase is driven by high rate cycling.[47]

In conclusion, this study provides evidence that the observed diamond-shaped Li-rich region within Li_xFePO_4 microcrystals at varying degrees of lithiation may correspond to the most energetically favorable distribution of phases at equilibrium, once the chemical driving force for the reaction is removed. Future work will focus on the extension of the methodology presented here to small particles and to examine the morphology dependence of the electrochemical phase transition.

Methods. *Single-Frequency IR s-SNOM Imaging.* Infrared imaging was performed with a NeaSNOM scanning near-field optical microscope (Neaspec GmBH). Platinum/iridium-coated cantilevered AFM probes (NanoAndMore GmbH; cantilever resonance frequency 250 kHz, nominal tip radius of curvature 20 nm) were scanned in tapping mode over the sample while illuminated by a focused infrared laser beam. The resulting backscattered radiation modulated by the tapping frequency (f_{tap}) interferes at a mercury-cadmium-telluride detector (Kolmar Technologies Inc.) with a reference beam whose phase is modulated continuously by reflection from an oscillating mirror (f_M). The pseudoheterodyne detection setup[16−18] utilizes demodulation of the overall IR signal at frequency side-bands $n f_{tap} \pm m f_M$ (for integers m and n) to supply the background-free amplitude (S_n) and phase[52] (φ_n) of the IR near-field signal at harmonics n of the probe tapping frequency. The near-exponential dependence of the near-field interaction versus the tip−sample separation distance implies that signal harmonics at $n \geq 2$ are directly attributable to near-field polarization of the tip in the case of harmonic tapping motion. Contrasts in intensity and phase at these near-field signal harmonics therefore correspond with variations in the local chemical composition of the sample.[53] An integration time of 6.5 ms per image pixel allowed fast raster-scan imaging of sample surfaces using tunable fixed-frequency quantum cascade lasers (Daylight Solutions Inc.). AFM topography and the mechanical phase of the probe oscillation were recorded simultaneously with all near-field IR images.

Nano-FTIR Spectroscopy. Single-point and line-scan near-field spectra were acquired using a NeaSNOM scanning near-

dx.doi.org/10.1021/nl5010898 | Nano Lett. 2015, 15, 1−7

field optical microscope operated at 80 nm probe tapping amplitude under illumination from a tunable broadband mid-infrared (700−2400 cm^{-1}) laser. This coherent mid-infrared light is generated through the nonlinear difference-frequency combination (through a GaSe crystal; DFG unit from Lasnix) of beams from two near-infrared fiber lasers (TOPTICA Photonics Inc.), a high power 5400 cm^{-1} oscillator and a tunable supercontinuum near-infrared amplifier, producing ∼100 fs mid-infrared pulses at a repetition rate of 40 MHz. An asymmetric Michelson interferometer with 1.5 mm range translating mirror enables the collection of demodulated near-field amplitude S_n and phase ψ_n spectra with 3 cm^{-1} resolution.[19,20] All nano-FTIR spectra are normalized to the nominally flat spectrum of the silicon substrate to remove the effect of frequency-dependent instrumental sensitivities and the incident illumination spectrum.

Modeling of near-Field Spectra. Near-field spectra were interpreted through comparison with solutions to the scattering equation describing optical interactions between an ideally conical conductive probe tip and a planar sample characterized by complex frequency-dependent dielectric function $\varepsilon = \varepsilon_1 + i\,\varepsilon_2$. This so-called lightning rod model[31] of realistic probe-sample near-field interaction computes the charge density per unit length $\lambda(z)$ induced along the vertical shaft of the tip from which both the magnitude and phase of the probe's backscattered field are computed semianalytically.

This model differs from earlier qualitative models primarily through the absence of ad hoc free parameters, explicit consideration of realistic probe tip geometries, and straightforward application to interactions with layered structures. Of key importance in determining the magnitude and phase of the induced charge $\lambda(z)$ and the associated backscattered radiation is the surface response function of the sample $\beta(\omega)$, equal to the quasi-electrostatic limit of the Fresnel reflection coefficient for p-polarized light illuminating a bulk material with frequency-dependent dielectric constant $\varepsilon(\omega)$[3,54]

$$\beta(\omega) = \frac{\varepsilon - 1}{\varepsilon + 1}$$

Intense backscattered radiation can result for large values of β near frequencies for which Re $\varepsilon(\omega) \approx -1$. For materials whose dielectric behavior is well described by a sum of vibrational oscillators, these frequencies (ω_{SO}) denote surface optical phonon modes of the lattice. The near-field resonance condition is satisfied at frequencies slightly red-shifted from ω_{SO}, providing spectral peaks in the backscattered s-SNOM signal that are the hallmark of these phonons. This forms the basis for an optical spectroscopy sensitive to changes in chemical composition at the nanoscale and well suited to the study of vibrational materials.

■ ASSOCIATED CONTENT

Supporting Information

Supporting Information for this work includes a detailed description of sample preparation, phonon calculations for $FePO_4$ and $LiFePO_4$, theoretical framework for nano-FTIR measurements, and phonon-enhanced near-field tomographic reconstruction of a partially delithiated Li_xFePO_4 microcrystal. This material is available free of charge via the Internet at http://pubs.acs.org.

■ AUTHOR INFORMATION

Corresponding Author

*E-mail: r_kostecki@lbl.gov.

Author Contributions

⊥I.T.L. and A.S.M. contributed equally to this work.

Notes

The authors declare no competing financial interest.

■ ACKNOWLEDGMENTS

This work (LBNL, Stony Brook, University of Cambridge) was supported as part of the Northeastern Center for Chemical Energy Storage, an Energy Frontier Research Center funded by the U.S. Department of Energy, Office of Science, Office of Basic Energy Sciences under Award Number DE-SC0001294. Work at UCSD was supported by U.S. Department of Energy, Office of Science, Office of Basic Energy Sciences. A.S.M. acknowledges support from a U.S. Department of Energy Office of Science Graduate Fellowship. We would like to acknowledge the helpful contribution of Simon F. Lux with the near-field IR imaging measurements. We thank the Center for Functional Nanomaterials, Brookhaven National Laboratory, NY, U.S.A., which is supported by the U.S. Department of Energy, Office of Basic Energy Sciences, under contract number DE-AC02-98CH10886 for access to their computer cluster.

■ REFERENCES

(1) Yamada, A.; Koizumi, H.; Nishimura, S.-i.; Sonoyama, N.; Kanno, R.; Yonemura, M.; Nakamura, T.; Kobayashi, Y. *Nat. Mater.* **2006**, *5*, 357−360.

(2) Ellis, B. L.; Lee, K. T.; Nazar, L. F. *Chem. Mater.* **2010**, *22*, 691−714.

(3) Keilmann, F.; Hillenbrand, R. *Philos. Trans. R. Soc. London, A* **2004**, *362*, 787−805.

(4) Delacourt, C.; Poizot, P.; Tarascon, J. M.; Masquelier, C. *Nat. Mater.* **2005**, *4*, 254−260.

(5) Gibot, P.; Casas-Cabanas, M.; Laffont, L.; Levasseur, S.; Carlach, P.; Hamelet, S.; Tarascon, J.-M.; Masquelier, C. *Nat. Mater.* **2008**, *7*, 741−747.

(6) Delmas, C.; Maccario, M.; Croguennec, L.; Le Cras, F.; Weill, F. *Nat. Mater.* **2008**, *7*, 665−671.

(7) Chen, G. Y.; Song, X. Y.; Richardson, T. J. *Electrochem. Solid State Lett.* **2006**, *9*, A295−A298.

(8) Chen, G. Y.; Song, X. Y.; Richardson, T. J. *J. Electrochem. Soc.* **2007**, *154*, A627−A632.

(9) Ramana, C. V.; Mauger, A.; Gendron, F.; Julien, C. M.; Zaghib, K. *J. Pow. Sources* **2009**, *187*, 555−564.

(10) Laffont, L.; Delacourt, C.; Gibot, P.; Wu, M. Y.; Kooyman, P.; Masquelier, C.; Tarascon, J. M. *Chem. Mater.* **2006**, *18*, 5520−5529.

(11) Sigle, W.; Amin, R.; Weichert, K.; van Aken, P. A.; Maier, J. *Electrochem. Solid State Lett.* **2009**, *12*, A151−A154.

(12) Meirer, F.; Cabana, J.; Liu, Y. J.; Mehta, A.; Andrews, J. C.; Pianetta, P. *J. Synchrotron Radiat.* **2011**, *18*, 773−781.

(13) Boesenberg, U.; Meirer, F.; Liu, Y.; Shukla, A. K.; Dell'Anna, R.; Tyliszczak, T.; Chen, G.; Andrews, J. C.; Richardson, T. J.; Kostecki, R.; Cabana, J. *Chem. Mater.* **2013**, *25*, 1164−1672.

(14) Chueh, W. C.; El Gabaly, F.; Sugar, J. D.; Bartelt, N. C.; McDaniel, A. H.; Fenton, K. R.; Zavadil, K. R.; Tyliszczak, T.; Lai, W.; McCarty, K. F. *Nano Lett.* **2013**, *13*, 866−872.

(15) Burba, C. M.; Frech, R. *J. Electrochem. Soc.* **2004**, *151*, A1032−A1038.

(16) Atkin, J. M.; Berweger, S.; Jones, A. C.; Raschke, M. B. *Adv. Phys.* **2012**, *61*, 745−842.

(17) Vaeziravani, M.; Toledocrow, R. *Appl. Phys. Lett.* **1993**, *62*, 1044−1046.

(18) Ocelic, N.; Huber, A.; Hillenbrand, R. *Appl. Phys. Lett.* **2006**, *89*, 101124.
(19) Keilmann, F.; Amarie, S. *J. Infrared, Millimeter, Terahertz Waves* **2012**, *33*, 479−484.
(20) Amarie, S.; Keilmann, F. *Phys. Rev. B* **2011**, *83*, 045404.
(21) Craig, I. M.; Taubman, M. S.; Lea, A. S.; Phillips, M. C.; Josberger, E. E.; Raschke, M. B. *Opt. Express* **2013**, *21*, 30401−30414.
(22) Huth, F.; Govyadinov, A.; Amarie, S.; Nuansing, W.; Keilmann, F.; Hillenbrand, R. *Nano Lett.* **2012**, *12*, 3973−3978.
(23) Wagner, M.; Fei, Z.; McLeod, A. S.; Rodin, A. S.; Bao, W.; Iwinski, E. G.; Zhao, Z.; Goldflam, M.; Liu, M.; Dominguez, G.; Thiemens, M.; Fogler, M. M.; Castro Neto, A. H.; Lau, C. N.; Amarie, S.; Keilmann, F.; Basov, D. N. *Nano Lett.* **2014**, *14*, 894−900.
(24) Zhang, L. M.; Andreev, G. O.; Fei, Z.; McLeod, A. S.; Dominguez, G.; Thiemens, M.; Castro-Neto, A. H.; Basov, D. N.; Fogler, M. M. *Phys. Rev. B* **2012**, *85*, 075419.
(25) Taubner, T.; Keilmann, F.; Hillenbrand, R. *Opt. Express* **2005**, *13*, 8893−8899.
(26) Ait-Salah, A.; Dodd, J.; Mauger, A.; Yazami, R.; Gendron, F.; Julien, C. M. *Z. Anorg. Allg. Chem.* **2006**, *632*, 1598−1605.
(27) Burba, C. M.; Frech, R. *Spectrochim. Acta, Part A* **2006**, *65*, 44−50.
(28) Hillenbrand, R.; Taubner, T.; Keilmann, F. *Nature* **2002**, *418*, 159−162.
(29) Porto, J. A.; Johansson, P.; Apell, S. P.; Lopez-Rios, T. *Phys. Rev. B* **2003**, *67*, 085409.
(30) Taubner, T.; Keilmann, F.; Hillenbrand, R. *Nano Lett.* **2004**, *4*, 1669−1672.
(31) McLeod, A. S.; Kelly, P.; Goldflam, M. D.; Gainsforth, Z.; Westphal, A. J.; Dominguez, G.; Thiemens, M.; Fogler, M. M.; Basov, D. N. *Phys. Rev. B* **2014**, *90*, 085136.
(32) Dovesi, R.; Orlando, R.; Civalleri, B.; Roetti, C.; Saunders, V. R.; Zicovich-Wilson, C. M. *Z. Kristallogr.* **2005**, *220*, 571−573.
(33) Dovesi, R.; Saunders, V. R.; Roetti, C.; Orlando, R.; Zicovich-Wilson, C. M.; Pascale, F.; Civalleri, B.; Doll, K.; Harrison, N. M.; Bush, I. J.; D'Arco, P.; Llunell, M. *CRYSTAL09 User's Manual*; University of Torino: Torino, 2009.
(34) Delacourt, C.; Rodriguez-Carvajal, J.; Schmitt, B.; Tarascon, J. M.; Masquelier, C. *Solid State Sci.* **2005**, *7*, 1506−1516.
(35) Yamada, A.; Koizumi, H.; Sonoyama, N.; Kanno, R. *Electrochem. Solid State Lett.* **2005**, *8*, A409−A413.
(36) Kildemo, M.; Hunderi, O.; Drévillon, B. *J. Opt. Soc. Am. A* **1997**, *14*, 931−939.
(37) Andersson, A. S.; Thomas, J. O. *J. Power Sources* **2001**, *97*−*8*, 498−502.
(38) Malik, R.; Zhou, F.; Ceder, G. *Nat. Mater.* **2011**, *10*, 587−590.
(39) Padhi, A. K.; Nanjundaswamy, K. S.; Goodenough, J. B. *J. Electrochem. Soc.* **1997**, *144*, 1188−1194.
(40) Srinivasan, V.; Newman, J. *J. Electrochem. Soc.* **2004**, *151*, A1517−A1529.
(41) Dargaville, S.; Farrell, T. W. *J. Electrochem. Soc.* **2010**, *157*, A830−A840.
(42) Cogswell, D. A.; Bazant, M. Z. *Nano Lett.* **2013**, *13*, 3036−3041.
(43) Prosini, P. P. *J. Electrochem. Soc.* **2005**, *152*, A1925−A1929.
(44) Cogswell, D. A.; Bazant, M. Z. *ACS Nano* **2012**, *6*, 2215−2225.
(45) Shapiro, D. A.; Yu, Y.-S.; Tyliszczak, T.; Cabana, J.; Celestre, R.; Chao, W.; Kaznatcheev, K.; Kilcoyne, A. L. D.; Maia, F.; Marchesini, S.; Meng, Y. S.; Warwick, T.; Yang, L. L.; Padmore, H. A. *Nat. Photonics* **2014**, *8*, 765−769.
(46) Meethong, N.; Huang, H. Y. S.; Speakman, S. A.; Carter, W. C.; Chiang, Y. M. *Adv. Funct. Mater.* **2007**, *17*, 1115−1123.
(47) Bai, P.; Cogswell, D. A.; Bazant, M. Z. *Nano Lett.* **2011**, *11*, 4890−4896.
(48) Singh, G. K.; Ceder, G.; Bazant, M. Z. *Electrochim. Acta* **2008**, *53*, 7599−7613.
(49) Sharma, N.; Guo, X.; Du, G.; Guo, Z.; Wang, J.; Wang, Z.; Peterson, V. K. *J. Am. Chem. Soc.* **2012**, *134*, 7867−7873.
(50) Liu, H.; Strobridge, F. C.; Borkiewicz, O. J.; Wiaderek, K. M.; Chapman, K. W.; Chupas, P. J.; Grey, C. P. *Science* **2014**, 344.
(51) Zhang, X.; van Hulzen, M.; Singh, D. P.; Brownrigg, A.; Wright, J. P.; van Dijk, N. H.; Wagemaker, M. *Nano Lett.* **2014**, *14*, 2279−2285.
(52) Carney, P. S.; Deutsch, B.; Govyadinov, A. A.; Hillenbrand, R. *ACS Nano* **2012**, *6*, 8−12.
(53) Raschke, M. B.; Lienau, C. *Appl. Phys. Lett.* **2003**, *83*, 5089−5091.
(54) Aizpurua, J.; Taubner, T.; García de Abajo, F. J.; Brehm, M.; Hillenbrand, R. *Opt. Express* **2008**, *16*, 1529−1545.